Title:

In Silico Reconstitution of Actin-Based Symmetry Breaking and Motility

Mark J Dayel[†⋆], Orkun Akin[‡], Mark Landeryou[¶], Viviana I Risca[♯], Alex Mogilner[§], R. Dyche Mullins[‡]

[†] Miller Institute for Basic Research in Science, University of California Berkeley

[¶] Department of Mechanical Engineering, University College London

[♯] Biophysics Graduate Group, University of California, Berkeley

[‡] Department of Cellular and Molecular Pharmacology, University of California San Francisco

[§] Departments of NPB and Mathematics, University of California Davis

⋆ To whom correspondence should be addressed. E-mail: markdayel@gmail.com

Running title: *In Silico* Reconstitution of Actin-Based Motility

Abbreviations: Arp: Actin Related Protein; APS: Accumulative Particle-Spring;

Keywords: Actin-based motility; Symmetry Breaking; Accumulative Particle-Spring model; Simulation; Elastic-gel model;

Abstract

Background: Eukaryotic cells assemble viscoelastic networks of crosslinked actin filaments to control their shape, mechanical properties, and motility. One important class of actin network is nucleated and crosslinked by the Arp2/3 complex and drives both membrane protrusion at the leading edge of motile cells and intracellular motility of pathogens such as *Listeria monocytogenes*. These networks can be reconstituted *in vitro* from purified components to drive the motility of micron-sized beads. **Methodology/Principal Findings:** We have combined *in vitro* experiments with numerical simulation to reconstitute the behavior of these motile actin networks *in silico* using an Accumulative Particle-Spring (APS) model. Building on the Elastic Gel Model, our APS model demonstrates simple intuitive mechanisms for symmetry breaking and sustained motility and explains observed transitions between smooth and pulsatile motion as well as subtle variations in network architecture caused by differences in geometry and conditions. Our findings validate the Elastic Gel model for symmetry breaking, extend it to explain smooth motility, show that a soap-squeezing mechanism is not necessary to drive motility, and explain the observed sideways symmetry breaking and motility of elongated beads.
Conclusions/Significance: The APS model not only mirrors our *in vitro* observations, but also makes novel predictions that we confirm by experiment, demonstrating how a small number of viscoelastic network parameters and construction rules suffice to recapture the complex behavior of motile actin networks.

Introduction

The directed assembly of actin networks controls the motility and mechanical properties of most eukaryotic cells [1]. Specialized cellular factors assemble actin into different network types, each with a unique architecture and cellular function. One of the most well studied actin assembly factors is the Arp2/3 complex, a seven-subunit protein complex that nucleates formation of new filaments from the sides of pre-existing filaments, to create an entangled, dendritic array of filaments. These entangled dendritic arrays behave like viscoelastic gels with an elasticity that depends on the degree of branching and which break or rip under relatively low stress [2, 3].

In vivo, dendritic networks built by Arp2/3 complex form the lamellipod at the leading edge of motile cells [2, 4] as well as the 'comet tails' whose assembly drives intracellular movement of endosomes [5, 6] and intracellular pathogens [7] such as Vaccinia virus [8] and *Listeria* [9]. Construction of these motile networks *in vivo* requires a set of highly conserved accessory proteins, including capping protein, cofilin, and profilin, that function together with the Arp2/3 complex in a simple biochemical cycle, converting monomeric actin into crosslinked polymer and back again [4, 10]. Motile, dendritic actin networks can also be constructed *in vitro* by recombining purified components of the actin assembly cycle at the proper concentrations [11-13]. These reconstituted actin networks have become a powerful tool for studying how individual protein-protein interactions control the large-scale behaviors of cytoskeletal systems.

The simplest way to initiate assembly of motile, dendritic actin networks *in vitro* is by using micron-sized beads coated with factors that activate the Arp2/3 complex. When added to the reconstituted actin assembly cycle, beads coated uniformly with Arp2/3 activators initially generate spherically symmetrical actin shells before 'breaking symmetry' and forming stable, asymmetrical comet tails that drive directed motion [11, 14]. Actin-based symmetry breaking is also required for motility of intracellular pathogens [15] and some migrating cells [16], and the biophysics of this process has been studied in some detail [reviewed in ref 17].

Several theoretical frameworks have been proposed to explain actin-based symmetry breaking and motility [reviewed in ref 18]. Some are based on microscopic descriptions of actin assembly and crosslinking [19, 20] while others take a more coarse-grained approach, based on the bulk mechanical properties of crosslinked polymer networks [17, 21-26]. One such coarse-grained model, generally referred to as the 'elastic gel model' [22, 23], provides intuitive explanations for both symmetry breaking and sustained motility. In this model, symmetry breaking occurs when new actin network, continuously deposited at the surface of the bead, displaces older portions of the network radially outward. Expansion of the older network stretches it like the surface of an inflating balloon, until, at a critical threshold, circumferential stress causes a rupture in the network (either by melting [25] or cracking [27] the shell) and breaks the symmetry of the system. This mechanism fits the experimental observations of symmetry breaking [11, 22] better than mechanisms inferred from filament-based descriptions of the network [20].

After breaking symmetry, the bead continues to move on an actin 'comet tail'. The elastic gel model suggests that a soap-squeezing mechanism might drive this movement [23], in which surface-associated polymerization stretches older network outwards (in a direction orthogonal to the direction of motion) storing energy which it releases by contracting, squeezing the bead and pushing it forward like a hand squeezing a wet bar of soap. Another characteristic of the bead motion on the comet tail is its steadiness. Both smooth and pulsatile motion occur in experiments, pulsatile motion suggested to result by an unstable balance between the pushing forces and the drag from attached filaments [21].

In this paper we examine the essence of actin-based bead motility by reconstituting it *in silico* from the network's fundamental viscoelastic properties. Just as reconstituting actin-based motility *in vitro* from a minimal set of purified protein components demonstrates their necessity and can show how they contribute to the large-scale behavior, reconstituting actin-based motility *in silico* allows us to demonstrate the necessity and specific contributions of a minimal set of higher-level network properties (e.g. elasticity, crosslinking, etc), and demonstrate the mechanisms of motility on a mesoscopic scale. To do this, we use a framework we call the Accumulative Particle-Spring model, in which the viscoelastic actin network is represented simply as a set of particles, subject to viscous drag, and coupled by springs that break when strained

beyond a certain limit. New Particle-Spring network is created at the bead surface, just as the *in vitro* actin network polymerizes at the bead surface [11], and this simple system is sufficient to reproduce a range of the behaviors of actin networks including symmetry breaking and motility.

We explore the dynamic behavior of these *in silico* networks and compare the results and predictions to *in vitro* experiments in which we reconstitute symmetry breaking and motility from purified proteins. We use speckle microscopy to follow the dynamic behavior of the *in vitro* actin networks during symmetry breaking and sustained motility and compare this to the behavior of our Accumulative Particle-Spring model.

Our simulations enable us to explore the feasibility of hypothesized mechanisms of force and movement generation, and determine the essence of the behavior by exploring the minimal requirements to produce the observed results. Among the questions we address are: (i) What are the stress and strain distributions in a growing symmetric actin shell, and in a comet-like tail? (ii) Does the 'soap squeezing' model drive motility? (iii) Where exactly is the symmetry break initiated (outer or inner surface of the actin shell), and what is the 3D structure and dynamics of the break? (iii) How and when is the site of symmetry breaking determined? (iv) What is the pushing versus pulling forces' distributions around the moving bead? (v) What determines the transition from smooth to pulsatile motility? And finally (vi) how does symmetry breaking occur for non-spherical objects?

Results

Viscoelastic forces drive Bead Motility

To perform our *in vitro* bead motility experiments, we evenly coated 5 μm diameter beads with ActA and added them to motility mix (see Methods). An actin network grows in a tightly localized zone at the bead surface, breaks symmetry, and propels the bead on actin 'comet tail' (Figure 1a—d and movie S1).

To find out how well bead motility can be explained simply by the viscoelastic properties of the network, we created a computational model that simulates the behavior of a generic viscoelastic network deposited stochastically at the surface of a bead (see Methods). With nucleation at a constant rate and with an even distribution across the bead surface, our simulations produce symmetry breaking behavior and motility that reproduces the sequence of events seen *in vitro* (Figure 1e--h, movie S2).

Our experimental observations and our simulations share several features. As the shell grows, it becomes denser near the surface of the bead. When the thickness of the shell reaches approximately the radius of the bead, a clear crack develops and the bead exits the shell, then the shell opens, crescent-like, and motility proceeds leaving a low density and somewhat irregular comet-like tail behind the bead. Figure 1i—l and movie S3 also show the underlying 3D nature of the simulated network, with the network links colored by tensile stress.

Geometry of Symmetry Breaking

Although the shell is usually a perfect arc in the experiments, the simulations robustly show a more V-like shape with a dent in the center (compare Figure 1 panels c and d with g and h). To determine the cause of the dent, we examined the 3D mechanics of symmetry breaking in our simulations. Figure 2a,b show 3D top and side views of a representative simulated shell after the

bead has moved away from the shell, demonstrating that even though the bead is unconstrained in 3 dimensions, the symmetry break and shell opening occurs along only one axis. Figure 2a also shows high strain (yellow and red stretched links) in the middle hinge region that corresponds to the dent in the shell (a corresponding Gaussian convolved view shown in Figure 2c). Figure 2d shows an earlier 3D view of the same simulation, just as the crack completely fractures the shell. Isosurfaces show (in green) the densest region of the network to highlight the shape of the shell, and (semi-transparent) the extent of the lower density actin network. The symmetry-breaking crack is a straight line, as opposed to either lightning-like fracture(s) along the weakest regions of the network, or a circular hole opening to allow the bead to escape. The consequence of this straight-line break is that the 3D stresses in the network are relieved in a 2D manner---essentially splitting the 3D spherical shell into 2 hemispheres that open apart from one another like a clamshell, causing large stresses at the hinge. When this 3D geometry is viewed from above, the hinge appears as a dent, seen in Figure 2a,c.

In our experiments, the bead is intentionally confined closely between the slide and coverslip to prevent it moving out of focus whilst data is taken, and we hypothesized that the perfect arc seen in the experiments might be a result of this constraint on the network. To test this we ran the same simulation while constraining the network between 2 planes (we also excluded nucleation from the very top and bottom 10% of the bead to prevent artifacts caused by this material having nowhere to go). Figure 2e and f correspond to 2c and d, but for this constrained shell. The constraint creates a toroidal shell that also breaks in a straight-line crack, but unlike the breaking of the spherical shell, the broken toroidal shell relaxes into an arc without the clear dent, and the shell more closely resembles those seen in the experiments.

Conversely, our simulations predict that for an unconstrained 3D volume *in vitro*, symmetry breaking would produce clamshell break with a dent in the shell opposite the break site. To test this we performed the *in vitro* experiment using 5 μm diameter ActA coated beads whilst controlling the headspace of the reaction with glass spacer beads of either 5.1 μm diameter for the constrained or 15.5 μm for the unconstrained condition. For confocal imaging, we fixed the reaction after symmetry breaking (see Methods) so experimentally we are only able to capture the 3D geometry at one time-point after symmetry breaking has occurred, in contrast to having every

time-point in the simulations. Figure 2g and h show an example of a 2D projection and 3D reconstruction of a confocal stack of an unconstrained bead, confirming the distinctive bi-lobed structure, and V-shaped shell with central dent. Figure 2i and j similarly show the constrained condition with the perfect arc (see Supplementary Materials Figure S8 and S9 for further examples of 2D projections and 3D reconstructions from experiments and Figure S11 for 3D models of simulations).

Shell Deformations during Symmetry Breaking

To confirm that not only the geometry, but also the mechanics of symmetry breaking in our simulations reflect those seen *in vitro*, we used Fluorescence Speckle Microscopy to track deformations in the shell during *in vitro* symmetry breaking (Figure 3a). Low doping of fluorescent actin produces fiduciary marks that allow us to measure the mechanical deformations of the network [28]. We tracked five parameters: bead displacement, expansion of the crack, circumferential stretching of the inner shell, circumferential stretching of the outer shell and radial stretching of the shell (Figure 3b,c). When symmetry breaks, the crack opens rapidly and then slows as the shell approaches its final shape. The start of bead movement is synchronous with opening of the shell, and the velocity is approximately constant throughout, even as the shell slows its opening. As the shell opens, the outer circumference contracts with kinetics that mirror the crack opening, but the inner shell remains approximately the same circumference, merely reducing its curvature. As the shell opens, it becomes thicker, with the kinetics of radial expansion mirroring the circumferential contraction and crack opening.

We plotted similar parameters for a simulation run. We measured the 3D distance between pairs of points randomly chosen to be in the symmetry-breaking plane and approximately 2 μm apart (e.g. outer radial lines shown in figure 3d, others with corresponding Movie S6). The mechanics of the simulations behave like the *in vitro* experiments, with the crack opening rapidly, the outer circumference of the shell contracting and the shell becoming radially thicker, all with similar kinetics. The behavior of the inner shell differs slightly, with the circumference transiently expanding a little before returning to its original length, while *in vitro* the length remains constant. The most likely reflects transient disequilibrium during the most rapid part of the

symmetry breaking which is equilibrated more quickly *in vitro* than in the simulations. N.B. In our simulations, 1 second corresponds to ~ 1.4 frames, but we keep 'frames' as the time unit for our simulations to make clear which figures refer to simulations, and stress that we have not yet kinetically calibrated the model.

Mechanics of Symmetry Breaking

Our simulations allow us access to detailed information about the mechanism of symmetry breaking, e.g. the network motion, distribution of forces and ripping of the network (Figure 4a--d, Movie S5). In the left panels we color the regions of the network with red stripes to show the trajectory of the network as it moves away from the bead surface. Initially (frames 1-60) this pattern is radially symmetric indicating symmetric motion of the network away from the bead, with broken links occurring randomly around the surface giving no indication of the future site of symmetry breaking (link breaks are stochastic, see Movie S3). By Frame 62 (Figure 4a), the nodes around the future crack site have begun to diverge (left panel), followed by localized link breakage at the site (Figure 4b). This in turn weakens the network, causing stress in that region to be distributed over fewer remaining links, leading to more breaks by positive feedback (Figure 4c), and the bead moves off with links breaking primarily in front of the bead (Figure 4d).

To determine the force balances that contribute to shell formation and symmetry breaking, we examined the spatial distribution of stresses within the network. The right hand graphs of figure 4a--d show how the radial and circumferential link tension vary with distance from the surface of the bead, and the center panels show spatial distribution of circumferential tension around the bead. At the surface, radial and circumferential link forces are equal and low (there is little tension at the surface of the bead, and it is homogenous). Circumferential tension, but not radial tension, increases linearly with distance from the bead up to ~1.0 μm. i.e. as the network is pushed out by nucleation at the center, circumferential tension provides the balancing force. Radial tension does not increase because, compressed by the circumferential tension, the network does not expand radially. Circumferential tension peaks at around 1.3 μm, and tails off at higher distances because the network becomes sparse. Prior to symmetry breaking, link breaks are non-cooperative and randomly distributed around the bead, primarily in the outer shell (~1.5—3 μm).

When the main symmetry breaking crack occurs the link breaks occur in the peak stress region at ~1.3um from the surface. Together these data suggests that the main contribution of the outer shell to symmetry breaking is indirect: a loose outer network compresses the inner network, increasing its density.

This force balance and pattern of link breaks before symmetry breaking defines the final curvature of the shell after symmetry has broken. Decreasing the spring constant between links of the network (the F_L parameter) means that more material must be deposited to build up enough circumferential tension for symmetry to break. This is demonstrated in Figure 4e, in which halving the spring constant causes the shell to double in thickness (c.f. Figure S17). Also, the final curvature of the shell after recoil is dependent on the number of links that have broken in the outer shell during the earlier stages of shell buildup. Increasing the threshold force for link breakage (the F_{LB} parameter in the simulation) causes the shell to become flat (Figure 4f), since without breaks in the outer shell, the final equilibrium area of the outer shell is still the same as the inner. These parameters and others are more thoroughly explored in Section S4 of the Supplementary Materials.

Small defects in the outer shell have been previously proposed to establish the site of symmetry breaking [24, 25], and our simulation allows us to determine the point at which symmetry breaking is established. In our simulations, we add new network stochastically at the bead surface---this randomness results in a unique network and symmetry breaking direction for each run. For each run we have a complete description of the system at each frame, and can resume the run at any point with a different random seed. To discover the time at which the symmetry breaking direction is determined, we ran a simulation through to symmetry breaking, then rewound and restarted the same simulation from 9 different time-points, but with a different random seed. We repeated this set of runs 5 times to calculate the mean and standard deviation of the angle between the new symmetry breaking direction and the original direction (Figure 4g). This should give a high variance in symmetry breaking direction before the direction is determined, and very low variance and zero deviance angle afterwards. We find the symmetry breaking direction is essentially random until frames 80 and 90 at which point the direction becomes the same as the original run. Symmetry breaking direction is therefore determined

between frames 70 and 80, i.e. very late, just before symmetry breaks and not early by defects in the initial outer network.

Symmetry Breaking and Network Plasticity

Symmetry breaking is a particularly robust behavior of the model. Of the parameters tested those that do not break symmetry are those that set network coherency to extremes. One extreme creates a very strong network that builds a dense shell that never breaks symmetry; specifically this requires conditions in which the network strength increases faster than the network strain (we can produce this when we increase the probability of forming links or the link strength, and remove the limit on links per node; c.f. Figure S14, S16 without this limit removed). The other extreme creates a very weak network in which symmetry does not break because chains of links are too short to communicate tension around the bead, and the network remains unpolarised. We can achieve this by decreasing the crosslinking probability, or decreasing the link-breaking threshold (Figure S14, S16). We find that even a low level of network coherency is sufficient to support symmetry breaking, the key being that tension is transmitted around the bead. This kind of symmetry breaking does not involve a distinct shell that cracks, but a gradual oozing of the bead from a network cloud.

This oozing demonstrates a qualitative change in behavior that results from the quantitative change in degree of crosslinking. When a sparsely linked network deforms it undergoes plastic flow as energy is lost by links breaking independently, while when a dense network deforms it builds up elastic energy, as each link stretches slightly whilst remaining below its breaking strain. Eventually this dense network undergoes brittle fracture when many links break at once.

Prior to symmetry breaking we observe an increase in network density from the outer to the inner surface of the shell in both *in vitro* and *in silico*. This density gradient emerges spontaneously from the APS model as a result of the increasing circumferential tension in the outer shell compressing the inner shell. The initial outer network is sparse because it is not under compression, so the network has a low density of links (since links are formed to nearby nodes, and a sparse network means fewer nodes nearby). This sparse initial outer network is weak and

plastic but does provide enough compression on the inner network to cause an increase in density, hence a greater number of links, and a stronger network, which builds by positive feedback. As demonstrated in Figure 4a—d, which shows a peak in circumferential tension towards the center at around 1.3 μm from the surface, it is this inner brittle network that stores the elastic energy, and undergoes brittle fracture during symmetry breaking.

Network Deformations During Smooth Motility

In both our experiments and simulations, the bead continues to move after breaking symmetry. A 'soap-squeezing' model [23] has been proposed to explain how propulsive force is generated during this motility. In this model, the network stretches orthogonally to the direction of motion as it is pushed away from the surface. This model proposes that the stretched network would contract orthogonally to the direction of motion as it moves further from the bead, squeezing the bead forwards. Consistent with this mechanism is the distortion of motile vesicles into a raindrop shape, suggesting side compressive and rear squeezing and drag forces [29].

The soap-squeezing model predicts that the network should first expand then contract orthogonally as it moves away from the bead. To test this we plotted orthogonal views of the network trajectory for a simulation of smooth motion (Figure 5a). We marked network with a spatiotemporal grid, coloring it red when it originated at evenly spaced positions around the bead (the parallel lines in the tail), and evenly spaced time pulses during the run (the orthogonal shell-like curves). During the smooth motion phase, we see a pattern of parallel lines behind the bead demonstrating that the network does not contract orthogonally as it moves away from the bead surface, and close inspection shows the lines immediately behind the bead to diverge very slightly. So in our simulations, orthogonal contraction of the network does not provide the driving force for motility by squeezing the bead forwards.

Network motion around the bead occurs primarily in one plane. Figure 5a shows that the tail is much wider in one axis than the other, similar to the shell during symmetry breaking in Figure 2a and b. In 3 dimensions (Figure 5b and Supplementary Information Figure S12), tracking the network trajectory shows ripping in one axis along a sustained straight-line crack at the front of

the bead. We confirmed that the trajectories of the network in our simulations match those seen *in vitro* using Fluorescence Speckle Microscopy. Figure 5c shows a composite image, produced by coloring and overlaying successive frames from a movie of a motile bead *in vitro*, registered to the motile bead (i.e. lines represent movement relative to the bead). The trajectories *in vitro* mirror those seen *in silico*, with network expanding away from the bead as it is swept around and incorporated into the tail. This sweeping motion exerts forces on the bead (shown in Figure 5d) that closely match the distribution of forces calculated to explain the raindrop-shape distortion of *in vitro* motile vesicles [29].

In Figure 5a, the time pulse markings shows regions of network that came from the bead surface within a short time, and in effect show what happens to the equivalent of 'shells' for the smooth motion. In the tail, they appear as bars of red with curvature much lower than the bead curvature, i.e., even during smooth motion, the high-curvature network produced at the bead is opening up just like the shell during symmetry breaking. This suggests that the network might contract circumferentially and expand radially as it is swept around the bead, as we saw during symmetry breaking in Figure 3. To test this we made similar measurements of the network stretching during smooth motion. Figure 5f and g (and movie S6) show the positions of circumferential and radial measurements during smooth motility. Similar to the symmetry-breaking measurements, circumferential measurements are between pairs of points ~2 μm apart that were created essentially simultaneously at the surface of the bead, i.e., in the smooth motion equivalent of a 'shell'. Figure 5h shows these measurements plotted as the bead moves, confirming that the network stretches circumferentially before relaxing back almost to its original length, and to expand radially as it does so---just like the outer shell during symmetry breaking. Why then, do the trajectory lines of the network look parallel (and even diverge slightly) as they move away from the bead? Although the network expands orthogonally to the direction of travel, the network on the outer edges of the tail sweeps backwards relative to the inner tail, bringing points of the network in the smooth motion equivalent of a 'shell' closer together (circumferential contraction).

Sustained Rip Model for Motility

Instead of soap-squeezing providing the driving force for motility, we propose a 'sustained rip'

model, which is a simple extension of the symmetry breaking mechanism, combined with a pressure-induced transition from brittle to plastic network behavior. As during symmetry breaking, network produced at the bead surface tends to be pushed outward creating circumferential tension (Figure 5g). During motility, however, the existing shell (or tail) reinforces the network at the rear, forcing circumferential tension to be relieved by stretching and ripping at front. The radial compression that balances the circumferential tension presses on the bead from all sides except where there is little network at the front (see Figure 5d, black lines), driving the bead forwards through the rip site. Ripping also means that radial compression does not build up enough to compress the network and cause it to become dense and brittle, so it remains sparse and plastic. Direction is maintained because contact with the tail (or the original shell) always reinforces the network at the back, leaving tension from the expanding network to be relieved by ripping in the unreinforced zone at the front. The network trajectories in Figure 4d support this, showing that contact with the original shell indeed restricts the new network from free expansion at the rear---the new network does not expand symmetrically as the original shell did in Figure 4a, but diverges less in the rear region in contact with the shell, and more at the front.

This sustained rip model predicts that specific changes in network properties will affect the continuity of motion. For example, after symmetry breaking, motility should be smooth only if the newly forming network is sparse and plastic when uncompressed. If the newly forming network has a high enough link density that it behaves like the brittle inner network of the original shell, we should see pulsatile motion---essentially repeated symmetry breaking as new brittle shells form one after another. This is an alternative to a previous explanation which suggests that friction between the network and the bead is the cause of pulsatile motion [21]. In our simulation, as new material forms it becomes part of the network by linking to existing nearby material. Changing the probability of forming network links (P_{XL}) is a simple way to test this prediction by altering the network link density.

We ran simulations to see how varying the probability of forming links affects the smoothness of motility. Figure 5h shows the network architecture at regular intervals and Figure 5i shows how bead velocity changes with time, for a range of max link probability (P_{XL}) values. At very low link probabilities (P_{XL} = 0.125), no coherent network forms and a symmetric cloud of material

surrounds a stationary bead. At P_{XL} = 0.375, symmetry breaks and the bead moves off. Under these conditions, there is no coherent shell that breaks symmetry and recoils; instead a diffuse cloud of material forms, and the bead gradually oozes from it. There are fluctuations in the velocity, but they remain small (<25% deviation from average velocity). As we increase P_{XL} to 0.625, a distinct shell forms, the bead undergoes one pulse after the initial symmetry break, and then the motion becomes smooth (<25% deviation from average velocity). As P_{XL} increases further to 0.875, the shell becomes denser, and the motion becomes very strongly pulsatile (>250% deviation from average velocity) and periodic, as repeated strong shells undergo largely independent symmetry breaking events. Bead velocity rises abruptly when the shell breaks, and tails off slowly as the shell relaxes, leading to an asymmetric velocity profile that closely matches experimental measurements of bead velocity during pulsatile motion [21]. This transition from smooth to pulsatile motion supports the sustained rip model for motility: As network coherency increases, the stronger shells formed are more immune to the influence of the previous shell, causing them to undergo essentially independent symmetry breaking. The small influence of the previous tail explains the relatively constant direction of motion.

Further supporting the sustained rip model, two other parameters of the APS model also control smoothness of motility by affecting the ability of the old network to alter the brittleness of the newly forming network: Increasing the node repulsive force makes the network less compressible, reducing the pressure-dependent density increase, and leading to smooth motion (Supplemental Material, Figure S18). Also, lowering the link spring constant F_L results in circumferential tension (and radial compression) building up more slowly, i.e. the network will have to get bigger before the dense, brittle shell forms, this causes a much thicker shell when symmetry breaks, thick enough to be beyond the effect of the initial tail, and immune from the sustained rip effect's ability to induce smooth motion (Supplemental Material, Figure S17).

Friction may also contribute to pulsatile motion: *in vitro* increasing surface ActA concentration (intended to increase the ActA-filament attachment component of friction) causes a transition from smooth to pulsatile motion [21]. We see a similar effect in our simulations: when we increase friction by increasing the strain limit before node-bead links break, we also see a transition from smooth to pulsatile motion (Supplemental Material Figure S20; note the transition

is less clear-cut than those described above). However, in the APS model we can show that friction is unnecessary for pulsatile motion, by eliminating node-bead links (i.e. zero friction), then inducing a transition from smooth to pulsatile motion (e.g. by increasing network coherency by increasing P_{XL}; Supplemental Material, Figure S23). We interpret this to mean that the change from smooth to pulsatile motion is directly caused by a change from a plastic to brittle network, and that a dense, brittle network can be caused by increasing its density in two ways, either 1) by increasing the coherency of the outer shell which puts pressure on the inner shell or 2) by increasing the network-bead attachment which increases the density of the inner shell by holding it close to the bead surface.

Capsule (*Listeria*-like) and ellipsoidal geometry

Listeria are capsule-shaped bacteria that have an asymmetric surface distribution of ActA, a protein that nucleates an actin network that propels the bacterium lengthwise on an actin comet tail. To determine the importance of shape and of nucleator distribution on motility, we tested the effect of varying them *in silico*. When we simulate a capsule-shaped nucleator with nucleation restricted to one half of the capsule, motility is lengthwise and symmetry breaking is unnecessary (Figure 5a—d). Network tracks with regular spacing and frequency (Figure 5c) and 3D tracks (Figure 5d) show that the network expands outward from the nucleator, opening up as it moves away from the surface. Similar to the motility of spherical beads, there is no evidence for orthogonal contraction of the network essential to a soap-squeezing mechanism.

When we distribute nucleation uniformly over the capsule surface, the direction of motion changes: For both symmetry breaking and motility the capsule moves sideway, as shown in top and side views in Figure 5e—h. The elastic gel model predicts that the higher the surface curvature, the faster the build up of strain within the network [22]. We therefore anticipated the higher curvature regions at the ends would build up strain faster and that symmetry breaking would occur there (the ends are higher curvature because although the radii are equal, the curvature is 2D at the ends but only 1D on the linear section). The reason this did not occur can be seen from the network tracks just prior to symmetry breaking shown in Figure 5i, in which the

network on the linear section is drawn towards the ends of the capsule, relieving the strain at the ends. Along its axis, the capsule is a cylinder, so the lack of a linear section provides no relief of strain build up and symmetry breaking occurs by a similar mechanism to the spherical geometry. To check this, we plotted the circumferential strain around the capsule long axis (Figure 5j) and orthogonally (Figure 5k) and found that the circumferential forces around the capsule axis are indeed much stronger than the orthogonal circumferential forces, explaining the sideways symmetry breaking, and motion by a sustained rip mechanism.

We checked our prediction of sideways symmetry breaking and motility by stretching spherical beads to make ellipsoids and comparing their *in vitro* motion with simulations. Figure 5l shows that simulations of ellipsoids produce the same sideways symmetry breaking seen for the capsules (subsequent motion is also sideways like the capsules, data not shown). We performed bead motility experiments as before, with a 15.5 μm headspace (i.e. unconstrained), and captured 3D z-stacks of the beads soon after symmetry breaking. Figure 5n and m show a 2D projection and 3D reconstruction of such an ellipsoidal bead experiment after sideways symmetry breaking, with two density isosurfaces: the green chosen to show the shell, and the semi-transparent grey chosen to outline the void space of the ellipsoidal bead to confirm the bead position and orientation. Note the difficulty in determining the direction of motion relative to the bead axis from the 2D projection alone. More examples are shown in the Supplementary Materials Figure S10. For ellipsoid aspect ratios > 1.75:1 we almost always see sideways symmetry breaking (98%, n=58) and sideways motion (95%, n=55), though we occasionally see beads changing direction or curved bead paths during the subsequent motion.

Discussion

In this study we show that a minimal set of viscoelastic network properties are sufficient to reconstitute actin-based motility *in silico*. Having gathered data on the behavior of the actin network during *in vitro* motility experiments and reconstituted this behavior *in silico*, we explored this *in silico* system to show how the network properties give rise to the behavior. We also found some novel behaviors e.g. sideways motion of ellipsoids, shell dents for 3D symmetry breaking, which we returned to the *in vitro* system to test with experiments. Experimentally confirming these novel predictions without having to re-tweak the model suggests that the model is not simply replicating the experimental data fed to it, but has captured the essence of a significant underlying mechanism of actin based motility.

The actin network as an elastic gel

Our simulations build on the 'elastic gel model' of symmetry breaking [22, 23], using an Accumulative Particle-Spring (APS) model to capture the mesoscopic viscoelastic properties of actin networks. The APS model represents these properties using a series of nodes and springs that allow us adjust a simple set of viscoelastic network parameters that correspond to mechanical properties of the *in vitro* network. For example, the repulsive force between nodes (F_R) roughly corresponds to the resistance of the network to compression, and the spring constant (F_L) roughly corresponds to the resistance to tension. The APS model also captures some network behavior as emergent properties. For example, as the network stretches circumferentially, links re-orient circumferentially to result in strain hardening, and compression of the inner network by the outer network increases the node and spring density resulting in more the more brittle behavior necessary to produce the symmetry breaking and transition from smooth to pulsatile motion seen *in silico* and *in vitro*.

The APS model builds the network from spring-node units that correspond to a particular mesoscopic mechanical behavior of crosslinked actin networks. We know a good deal about the

viscoelastic behavior of *in vitro* actin networks from studies that examine the randomly crosslinked networks produced by mixing crosslinking proteins with stabilized actin filaments. For these networks, crosslinking proteins connect adjacent filaments with one another to form chains with a characteristic mesh size that can resist tension across the sample. The chains of nodes and springs *in silico* approximate the behavior of these chains of filaments, crosslinks and friction to transmit tension around the *in silico* bead. For Arp2/3-built networks to transmit tension around the bead implies significant friction and entanglement. Activated at the bead surface by ActA, Arp2/3 binds to existing filaments and nucleates new filaments from their sides to form a dendritic branched structure [2, 3]. Because only new filaments are crosslinked, each dendritic tree cannot crosslink to any other, so there can be no encircling chains of filaments and crosslinks around the bead that could carry tension. Circumferential tension would simply be dispersed by separation of these independent dendritic networks were it not for friction and entanglement. The node-spring links in our APS model therefore also implicitly represent these friction and entanglement links between dendritic trees, and just as friction and entanglement would be expected to increase with network density and pressure, so the the density of node-spring links in the APS model increase with density and pressure.

Symmetry breaking 3D geometry

In an expanding shell the actin network continuously stretches as it is displaced outward by assembly of new actin at the surface. The opening of the shell during symmetry breaking is well explained by the basic assumption of the elastic gel model: that all network layers tend to relax to their equilibrium area, the area of the surface of the bead where they were created. Since this area is the same for all layers, and since connected layers with equal areas and a non-zero thickness would tend to flatten to a plane, the shell tends to flatten towards a plane once symmetry breaks. For most conditions we don't see perfectly flat plane, but we do see the shell relax to a flat plane when we increase the link strength. This is because high link strength reduces the number of links that break stochastically in the initial outer shell before symmetry breaking—-links only break during the actual symmetry breaking event. This explains the arc of the symmetry breaking shell: Before symmetry breaking, as the outer shell is stretched, links break irreversibly, expanding the equilibrium area of the outer shell, so the final shell shape is no

longer the relaxation of planes of equal equilibrium areas. The larger equilibrium area of the outer plane results in a convex shell.

The APS model also shows how the rip that occurs during symmetry breaking brings about the 3D geometry of the shell. Since the starting geometry is a sphere, as the shell opens and flattens, large tensile strains occur around the circumference (Figure 6a). Rips relieve these circumferential strains; one rip will produce a bi-lobed structure, but multiple cracks are possible (and observed) as the network strength is increased. In line with a previous experimental observation [27], our simulations show linear cracks (instead of a round hole opening to release the bead). These are linear rather than circular because positive feedback concentrates the strain to regions of high curvature [30]. The resulting cracked-shell geometry is reminiscent of the Mollweide projection of the globe, in which linear cuts in the map allow a 3D sphere to be flattened to a plane and reduce stretching distortions at the poles.

Compression, network coherency and pulsatile motion

Paradoxically, pulsatile motion is relatively simple---it is essentially repeated symmetry breaking---while smooth motion is more complex. The very same biochemical conditions build an initial rigid brittle shell that cleanly and distinctly breaks symmetry, and then builds a more plastic tail on which the bead moves smoothly. How does the presence of the old shell cause adjacent new network to behave in a plastic manner, and prevent another rigid shell forming to allow smooth motion? Our simulations suggest that this switch to plastic behavior rests on the pressure dependence of network plasticity. By reinforcing one side of the newly forming network, the old shell focuses the circumferential tensile strain on a small region of newly forming, uncompressed, and therefore plastic network on the other side, which rips. Key to this 'sustained rip' mechanism is that the ripping prevents pressure building up, so the network remains sparse and plastic, leading to continued ripping and steady-state smooth motion. If this pressure dependence is disrupted or reduced, the transition to smooth motion is delayed or abolished. Increasing P_{XL} increases the number of links and the coherency of the shell, leading to essentially independent shells and pulsatile motion.

We expect this pressure dependence mechanism to translate to the physical mechanisms for the switch to smooth motion seen in real actin networks, through pressure-dependent increases in entanglement, friction, and filament orientation effects (which is likely to be significantly affected by pressure, since load-directed filaments stall). Oblique filaments would tend to entangle and reinforce the network whilst contributing little to the movement of the bead away from the network, and so this may tip the system into a positive feedback of network stiffening that is relieved only by symmetry breaking. We predict a significant alignment of filaments orthogonal to the direction of motion for a pulsatile bead, but alignment in the direction of motion for a smoothly motile bead.

Another type of pulsatile motion is seen for Listeria and occurs on a much smaller scale, with steps of ~5.4 nm [19, 31]. Unlike the pulsatile motion described above, whose steps are of the order of the bead size, these 'nano-saltations' are very likely to be directly caused by friction because their scale is of the order of actin monomers, much smaller than the characteristic scale of the elastic gel properties of the network.

Site selection during symmetry breaking

Our prediction that the outer network is more flexible and plastic and the inner network more rigid and brittle has implications for the mechanism of symmetry breaking. The driving force behind symmetry breaking is the circumferential stretching of the network as it moves outward, and we initially expected to see a brittle crack in one region of the outer network that would seed the symmetry break, as has been previously proposed [24, 25]. We do not see this because the outer network is not brittle, but rather observe a generalized breaking of links scattered randomly over the whole surface.

If stochastic variations in the density of the initial (outer) layers of the network were to determine the symmetry breaking direction, we would expect the symmetry breaking direction to be determined early, when this initial network forms. We show that symmetry breaking direction is determined late, just before the rip occurs, implying that there is no existing vulnerability in the outer network that later seeds the crack, but rather that network density and linking are finely

balanced up to the critical point when load becomes too great, and failure occurs stochastically. This fits well with the mechanism proposed above for curved vs flat shells: the balanced stochastic breaking of links in the outer network not only equilibrates the strain, but results in the even expansion of the outer shell equilibrium area that leads to curved shells.

Mechanism of motility

Contraction of the network orthogonal to the direction of motion (soap squeezing) has previously been proposed as the mechanism that drives motility [23]. Our data show that although the bead experiences squeezing forces consistent with data from motile lipid vesicles, there is no orthogonal contraction of the network after the bead has moved forward. There is, however, contraction of the network circumferentially around the bead as during symmetry breaking. This maintains some similarity to the soap-squeezing model, in the sense that the network away from the bead contracts circumferentially, but the network does not directly squeeze the bead forward.

Our data suggest a simple way to look at bead motility: as an extension of symmetry breaking. The network behaves in a remarkably similar way during both symmetry breaking and motility, with both sharing a linear crack, network motion primarily within one plane, and radial stretching and circumferential contraction of the network as it moves away from the bead. The same build up and release of elastic energy, in the form of circumferential stretching of the network, drive both symmetry breaking and motility. Smooth motility is essentially the mechanism of symmetry breaking operating in steady-state, with directionality maintained by the reinforcement of new network at the back of the bead by the old shell or tail restricting the rip to the front.

Capsule (and ellipsoid) symmetry breaking

We find that the elastic gel model helps explain the sideways symmetry breaking and motility of capsule-shaped and ellipsoidal nucleators. The network stretches around the long axis to relieve the circumferential tension, so only around the short axis does tension buildup cause symmetry breaking (and motility) in the sideways direction. Our experiments using ellipsoids confirm this behavior *in vitro*, and support the elastic gel mechanism as the determinant of symmetry breaking

and motility behavior.

We show that for lengthwise symmetry breaking and motility, a capsule geometry requires asymmetric nucleation. Wild-type Listeria is capsule-shaped, moves lengthwise and has such an asymmetric distribution of its ActA nucleation factor [32, 33], but a deletion mutation of ActA has been identified that results in a 'skidding' sideways motion of Listeria in vivo [34]. Our data raise the possibility that the effect of this mutation could be to alter the asymmetric distribution of ActA activity.

Model Limitations

We have limited the scope of this study to the viscoelastic network properties, and aimed to make our simulation as simple as possible 1) to reduce the number of model variables and 2) so the simulations run quickly. Using a simple model with a small number of variables makes interpreting the results easier. We have a few network parameters (elasticity, connectedness, strength) that can be intuitively connected to the parameters. Having the simulations run quickly allows us to run a very large number of simulations, test the effect of changing each of the parameters, determine which behaviors of the system are robust, and learn about the mechanisms that produce the behavior by seeing how they break down at the extremes.

An inherent limitation of our model is that without explicit filaments we miss any filament specific effects (e.g. elastic Brownian ratchet, filament orientation effects). To include this would slow our simulations to a point where we could not explore its range of behaviors. Another simplification is that we treat the drag very simply: the system is over-damped, with drag proportional to velocity relative to the reference frame (consistent with a low Reynolds number regime). This limits our ability to quantify forces, but we have omitted internal drag relative to network, drag relative to fluid, and fluid motion because of their complexity, and the relatively good fit to experimental data we achieve without the internal drag.

Our approach contrasts with that of Alberts and Odell who created the first three-dimensional computer simulation of actin-based, Listeria motility [19] by modeling the behavior of large

numbers of individual actin filaments and branches. The Alberts-Odell model provided an important insight into the connection between the micro-scale behavior of individual filaments and larger-scale behavior of motile networks, namely how the buildup and breakage of filament-load attachments can produce 'nano-saltations' in motility similar to those observed experimentally [31]. To make their model computationally tractable, Alberts and Odell modeled actin filaments as inflexible rods, fixed rigidly in space soon after nucleation. Thus, the actin network in their model is an inelastic solid and could not be used to study processes involving elastic energy storage, plastic deformation, or mechanical failure. For example, the Alberts-Odell model could not be used to study mechanical symmetry breaking or the role of soap squeezing in sustained motility. Conversely, our APS model does not explicitly address how the actin network is generated from individual actin filaments and could not easily be adapted to study how the properties of individual filaments contribute to mechanics or motility.

Conclusion

The APS model demonstrates how simple viscoelastic properties of the *in silico* reconstituted actin gel give rise to the observed dynamics of symmetry breaking and steady and pulsatile motility of spherical, capsule-shaped and ellipsoidal objects coated with actin-nucleation factors. Future refinements of the model, calibrated with time, length and force data will allow quantitative estimates of internal actin network parameters (e.g. force, elasticity) that are not directly measureable. The model should also help investigate other physical cell phenomena that, though complex, may be dominated by similar relatively simple viscoelastic behaviors, e.g. lamellipodia, pseudopodia and septation, by including interactions with the cell membranes, anisotropic networks and contractile proteins found in vivo.

Acknowledgments

M.J.D gratefully acknowledges the support of a postdoctoral fellowship from the Miller Institute for Basic Research in Science. This work was also supported by the UCSF/UCB Nanomedicine Development Center and by grants from the NIH (RO1 grant GM61010) and the Sandler Family Supporting Foundation to RDM. It was also supported by NIH grant U54 GM64346 and NSF grant DMS-0315782 to A.M, and a University of California Systemwide Biotechnology Research & Education Program GREAT Training Grant 2007-14 to V.I.R. V.I.R. also gratefully acknowledges the support of the Paul and Daisy Soros Fellowship for New Americans. Our thanks to the Computer Graphics Laboratory, Greg Couch and Matt Harrington at UCSF for technical help and computing resources. We are also very grateful to Kurt Thorn for help with the confocal imaging, and M.J.D. gratefully acknowledges Erik Hom and Ken Dill for helpful discussions and encouragement when first beginning the project.

Materials and Methods

Computational model

A brief overview of the model is given here (more details are available in the Supplementary Materials Sections S5—S8). We simulate the network using a discrete-element approach, i.e. the actin network is represented as network of nodes in 3D space held together by links (Supplementary Material, Figure S24, S25). This is unlike a finite element approach, in which the mesh is a way to reduce the dimensionality of a continuum problem into finite number of equations (elements). Rather, network links and the effective mesh size that results are important properties of the network. Network links also have no direct correspondence to actin filaments, but rather the bulk viscoelastic properties of the network of links and nodes are intended to capture the bulk viscoelastic network properties of the actin network. Under the polymerization conditions used (i.e. in the absence of crosslinking proteins) nodes more properly correspond to entanglement of filaments, and links correspond to the elastic properties of the network. We model these links as simple linear springs with a defined breaking strain, and an inverse square repulsive force between nodes models the compression resistance of the material. We explicitly avoid the unresolved question of how polymerizing filaments behave on a molecular level at the nucleator surface (Brownian ratchet etc, [35, 36]), and model polymerization as the stochastic introduction of material (nodes) at constant rate at the nucleator surface. Once introduced, new nodes form links with their neighbors, with a higher probability of forming links with nearby nodes (linear tail-off with distance, max probability P_{XL} at zero distance), and a limit on the maximum number of links. Nodes at the surface of the bead are also linked to the bead at their last contact point by a link with force proportional to its length. Forces are calculated iteratively, and since this is a low Reynolds number regime, there is no inertia (i.e. velocity is proportional to force.)

Computational details

The computational model is implemented in C++, and run-times to symmetry breaking are ~1-2h

on a typical desktop computer. The code is designed to use concurrent processing to enable large-scale problems to be explored across a number of parameter regimes (runs typically involve 10^5 nodes, 10^6 links, and 10^6 iterations per simulation). The code is made freely available under an open source license to allow the results to be reproduced, to convey the full details of the model and to encourage further use of the code by other researchers. A detailed explanation of the details of the code and the parameter control file are provided in the supplementary materials.

In silico Visualization

To visualize the results of the simulations in a way comparable to *in vitro* microscopy images, we calculate the symmetry breaking plane, and create a 2D projection of the nodes of the network convolved with a Gaussian to represent the point spread function of the microscope.

Bead Motility Experiments

Bead motility experiments were carried out as previously described [11], with modifications. Briefly, 5 μm diameter carboxylated polystyrene beads (Bangs Laboratories Inc., Fishers, IN) were covalently coated with ActA. The motility mix contained 0.5 mM ATP, 1 mM $MgCl_2$, 1 mM EGTA, 15 mM TCEP-HCl, 50 mM KOH (to neutralize TCEP-HCl), 20 mM HEPES (pH 7.0), 125 nM Arp2/3 complex, 100 or 120 nM capping protein, and 3 μM actin. To aid microscopic observation, we included 3 mg/mL BSA (A0281, Sigma-Aldrich, St. Louis, MO) and 0.2% methylcellulose (M0262, Sigma-Aldrich). We controlled the headspace by adding 0.1% v/v 5.1 μm or 15.5 μm diameter glass spacer beads (Duke Scientific, Palo Alto, CA) prior to starting the reaction. For 3D reconstructions, reactions were stopped before imaging by adding 50% volume of 15 μM phalloidin and 15 μM Latrunculin B (Sigma-Aldrich, St. Louis, MO). Fluorescent speckle microscopy (Figure 3a) conditions: 7.5 μM actin (1/3000 TMR-labeled), 3 μM profilin, 40 nM Arp2/3, and 56 nM capping protein.

For the ellipsoidal bead experiments, spherical beads were stretched as previously described [37] with the following modifications: 140 μL of polystyrene bead stock was suspended in 6 mL of 3.8% w/v suspension of polyvinyl alcohol (PVA). The PVA/bead suspension was degassed before

casting films in a 4.5 x 7.0 cm leveled tray. After stretching, the PVA was dissolved by incubating at 90°C for 2 hours in distilled water containing 0.1% NP-40. The beads were washed three times in isopropanol and dried in a rotary evaporator. The bead surface was re-functionalized by incubation in 50% (w/v) NaOH for 1 hr at 90°C and overnight at 42°C, washed once with 20 mM Tris HCl pH 8.0 and 0.1% NP-40, and three times with 0.1% NP-40 before coating with ActA.

References

1. Pollard, T.D., W.C. Earnshaw, and J. Lippincott-Schwartz, *Cell biology*. 2nd ed. 2008, Philadelphia: Saunders/Elsevier. xix, 905 p.
2. Mullins, R.D., J.A. Heuser, and T.D. Pollard, *The interaction of Arp2/3 complex with actin: nucleation, high affinity pointed end capping, and formation of branching networks of filaments.* Proc Natl Acad Sci U S A, 1998. **95**(11): p. 6181-6.
3. Nakamura, F., et al., *Comparison of filamin A-induced cross-linking and Arp2/3 complex-mediated branching on the mechanics of actin filaments.* J Biol Chem, 2002. **277**(11): p. 9148-54.
4. Iwasa, J.H. and R.D. Mullins, *Spatial and temporal relationships between actin-filament nucleation, capping, and disassembly.* Curr Biol, 2007. **17**(5): p. 395-406.
5. Merrifield, C.J., et al., *Endocytic vesicles move at the tips of actin tails in cultured mast cells.* Nat Cell Biol, 1999. **1**(1): p. 72-4.
6. Taunton, J., et al., *Actin-dependent propulsion of endosomes and lysosomes by recruitment of N-WASP.* J Cell Biol, 2000. **148**(3): p. 519-30.
7. Gouin, E., M.D. Welch, and P. Cossart, *Actin-based motility of intracellular pathogens.* Curr Opin Microbiol, 2005. **8**(1): p. 35-45.
8. Frischknecht, F., et al., *Actin-based motility of vaccinia virus mimics receptor tyrosine kinase signalling.* Nature, 1999. **401**(6756): p. 926-9.
9. Tilney, L.G. and D.A. Portnoy, *Actin filaments and the growth, movement, and spread of the intracellular bacterial parasite, Listeria monocytogenes.* J Cell Biol, 1989. **109**(4 Pt 1): p. 1597-608.
10. Bear, J.E., et al., *Antagonism between Ena/VASP proteins and actin filament capping regulates fibroblast motility.* Cell, 2002. **109**(4): p. 509-21.
11. Akin, O. and R.D. Mullins, *Capping protein increases the rate of actin-based motility by promoting filament nucleation by the Arp2/3 complex.* Cell, 2008. **133**(5): p. 841-51.
12. Loisel, T.P., et al., *Reconstitution of actin-based motility of Listeria and Shigella using pure proteins.* Nature, 1999. **401**(6753): p. 613-6.

13. Upadhyaya, A. and A. van Oudenaarden, *Biomimetic systems for studying actin-based motility.* Curr Biol, 2003. **13**(18): p. R734-44.

14. Wiesner, S., et al., *A biomimetic motility assay provides insight into the mechanism of actin-based motility.* J Cell Biol, 2003. **160**(3): p. 387-98.

15. Rafelski, S.M. and J.A. Theriot, *Bacterial shape and ActA distribution affect initiation of Listeria monocytogenes actin-based motility.* Biophys J, 2005. **89**(3): p. 2146-58.

16. Yam, P.T., et al., *Actin-myosin network reorganization breaks symmetry at the cell rear to spontaneously initiate polarized cell motility.* J Cell Biol, 2007. **178**(7): p. 1207-21.

17. Paluch, E., et al., *Deformations in actin comets from rocketing beads.* Biophys J, 2006. **91**(8): p. 3113-22.

18. Mogilner, A., *On the edge: modeling protrusion.* Curr Opin Cell Biol, 2006. **18**(1): p. 32-9.

19. Alberts, J.B. and G.M. Odell, *In silico reconstitution of Listeria propulsion exhibits nano-saltation.* PLoS Biol, 2004. **2**(12): p. e412.

20. van Oudenaarden, A. and J.A. Theriot, *Cooperative symmetry-breaking by actin polymerization in a model for cell motility.* Nat Cell Biol, 1999. **1**(8): p. 493-9.

21. Bernheim-Groswasser, A., J. Prost, and C. Sykes, *Mechanism of actin-based motility: a dynamic state diagram.* Biophys J, 2005. **89**(2): p. 1411-9.

22. Bernheim-Groswasser, A., et al., *The dynamics of actin-based motility depend on surface parameters.* Nature, 2002. **417**(6886): p. 308-11.

23. Gerbal, F., et al., *An elastic analysis of Listeria monocytogenes propulsion.* Biophys J, 2000. **79**(5): p. 2259-75.

24. John, K., et al., *Nonlinear study of symmetry breaking in actin gels: implications for cellular motility.* Phys Rev Lett, 2008. **100**(6): p. 068101.

25. Sekimoto, K., et al., *Role of tensile stress in actin gels and a symmetry-breaking instability.* Eur Phys J E Soft Matter, 2004. **13**(3): p. 247-59.

26. Cameron, L.A., et al., *Biophysical parameters influence actin-based movement, trajectory, and initiation in a cell-free system.* Mol Biol Cell, 2004. **15**(5): p. 2312-23.

27. van der Gucht, J., et al., *Stress release drives symmetry breaking for actin-based movement.* Proc Natl Acad Sci U S A, 2005. **102**(22): p. 7847-52.

28. Waterman-Storer, C.M., et al., *Fluorescent speckle microscopy, a method to visualize the dynamics of protein assemblies in living cells.* Curr Biol, 1998. **8**(22): p. 1227-30.

29. Giardini, P.A., D.A. Fletcher, and J.A. Theriot, *Compression forces generated by actin comet tails on lipid vesicles.* Proc Natl Acad Sci U S A, 2003. **100**(11): p. 6493-8.

30. Anderson, T.L., *Fracture mechanics : fundamentals and applications*. 3rd ed. ed. 2005, Boca Raton, Fla. ; London: Taylor & Francis. 621 p.

31. Kuo, S.C. and J.L. McGrath, *Steps and fluctuations of Listeria monocytogenes during actin-based motility.* Nature, 2000. **407**(6807): p. 1026-9.

32. Rafelski, S.M. and J.A. Theriot, *Mechanism of polarization of Listeria monocytogenes surface protein ActA.* Mol Microbiol, 2006. **59**(4): p. 1262-79.

33. Niebuhr, K., et al., *Localization of the ActA polypeptide of Listeria monocytogenes in infected tissue culture cell lines: ActA is not associated with actin "comets".* Infect Immun, 1993. **61**(7): p. 2793-802.

34. Lauer, P., et al., *Construction, characterization, and use of two Listeria monocytogenes site-specific phage integration vectors.* J Bacteriol, 2002. **184**(15): p. 4177-86.

35. Mogilner, A. and L. Edelstein-Keshet, *Regulation of actin dynamics in rapidly moving cells: a quantitative analysis.* Biophys J, 2002. **83**(3): p. 1237-58.

36. Mogilner, A. and G. Oster, *Cell motility driven by actin polymerization.* Biophys J, 1996. **71**(6): p. 3030-45.

37. Ho, C.C., et al., *Preparation of Monodisperse Ellipsoidal Polystyrene Particles.* Colloid and Polymer Science, 1993. **271**(5): p. 469-479.

Figure Captions

Figure 1: Simulations mimic *in vitro* bead motility behavior. (a–d) *in vitro* symmetry breaking and motility for beads uniformly coated with ActA (e–h) computer simulation of symmetry breaking and motility (2D projections convolved with Gaussian) (i–l) 3D view of simulation showing links colored by tensile stress (color bar range represents zero to breakage stress).

Figure 2: The 3D geometry of symmetry breaking. (a,b) top and side views of simulated network show that symmetry breaking is along one axis only. (c) 2D projection of unconstrained simulation after symmetry breaking shows dent in the center of the shell (d) 3D isosurface representation of network and bead during symmetry breaking shows linear crack. (e,f) Same as a,b but constrained to a 2D slice (note absence of dent in shell) (g–j) *in vitro* projections and 3D reconstructions of experimental data after symmetry breaking (g–h) 5 μm bead with 15.5 μm spacers, (i–j) 5 μm bead with 5.1 μm spacers.

Figure 3: Shell deformations during symmetry breaking. (a) Fluorescence Speckle Microscopy (FSM) of *in vitro* symmetry breaking, timepoints as indicated (b) Diagram of geometric parameters extracted from FSM data. (c) Geometric parameters of *in vitro* symmetry breaking. (d) Diagram of outer circumference parameter extracted from simulation. (e) Geometric parameters of simulation of symmetry breaking.

Figure 4: The mechanism of Symmetry Breaking. (a–d) Strain buildup and release by link breakage. For 4 timepoints, images show node tracks, link breaks and circumferential (transverse) forces. Graphs on right show corresponding circumferential and radial link force buildup and broken links as functions of distance from the surface of the bead. (e) Decreasing the network spring constant increases the thickness of the shell (LINK_FORCE=1.5) (f) Increasing the threshold for link breakage produces a flat shell (LINK_BREAKAGE_FORCE=5.5) (g) Symmetry breaking direction is determined late. One simulation was repeated restarting at times shown, and the angle of the new symmetry breaking direction calculated relative to the original direction (mean ± SD, n=5). The direction is essentially random until frame 80.

Figure 5: The mechanism of motility. (a) Orthogonal views of the network trajectory for a

simulation of smooth motion, with network marked red at even intervals of time and position around the bead. (b) Orthogonal 3D views of the network trajectory show linear ripping at front (c) network tracks from *in vitro* motility: composite of sequential fluorescence speckle microscopy images colored by time. (e,f) positions of circumferential and radial measurements for smooth motion (g) graph shows circumferential stretching and contraction, and radial stretching of the network as it moves away from the bead. (h,i) varying degree of network crosslinking (P_{XL}) causes transition from smooth to pulsatile motion.

Figure 6: Simulation predicts sideways symmetry breaking and motility for symmetrically coated *Listeria* and ellipsoids. (a–d) Simulation with nucleation localized to only one half shows motion in the direction of the long axis of the *Listeria*. (c) Regularly spaced and timed speckle tracks show trajectory and deformations of the network. (d) 3D network trajectory (e–h) Simulation of uniformly nucleating *Listeria* shows sideways symmetry breaking and motility (side and top view of same run shown) (i) network trajectory prior to symmetry breaking (j,k) Circumferential (tangential) link forces around the capsule split into components in the directions shown (plotted to the same scale) (l) 3D view of ellipsoid simulation after symmetry breaking (m) 2D projection and (n) 3D reconstruction of *in vitro* ellipsoid experiment after symmetry breaking

Figure 7: Model for symmetry breaking and motility. (a) 3D Mechanics of symmetry breaking. (i) The network grows symmetrically until (ii) circumferential tension tears the load-bearing inner network and a linear crack forms in the shell. The crack propagates through the shell in a straight line at the points of high curvature (arrows). (iii) The crack propagates towards the rear of the shell (arrows), creating a weak point opposite the direction of motion, this point acting as a hinge. (iv) The two lobes of the shell open in a plane (curved arrows) about this hinge, allowing the bead to escape. (b) Forces and site selection during symmetry breaking. (i) A loose network polymerizes at the surface of the bead and is pushed racially outward. (ii) Radial expansion causes the outer network to expand and creates circumferential tension, causing random small rips around the outer shell. This circumferential tension also compresses the inner network, increasing its density and creating a more rigid brittle inner shell. Within this inner shell, a spherical shell (slightly away from the bead surface, shown in red) carries most of the circumferential tension. (iii) Circumferential tension is well balanced in this inner shell and continues to build until a stochastic break and positive feedback cause catastrophic failure. (iv)

The shell opens, with the outer network (O) contracting, the dense inner network (I) changing curvature but not expanding or contracting, and the shell expanding in the radial direction (R). (c) Sustained rip model for smooth motility. (i) After symmetry breaking new network (shown in blue) polymerizes at the surface of the bead. Contact with the original shell (R) reinforces the network at the back, leaving a thinner weaker area of network at the front (W). As the new network expands radially, it creates circumferential tension, which rips through the weaker area at the front and the bead moves forwards. (ii) The existing network (R) at the back continues to reinforce new network (blue), maintaining the weak area (W) at the front of the bead. This weak area is sufficiently weak that ripping occurs before enough circumferential tension builds up to reinforce the shell and create a rigid inner region (compare with b(ii) above) (iii) This continues, with the tail rather than the original shell maintaining the rear reinforcement, and the bead moving at steady-state constant velocity through a sustained rip at the front of the bead.

Figure 1

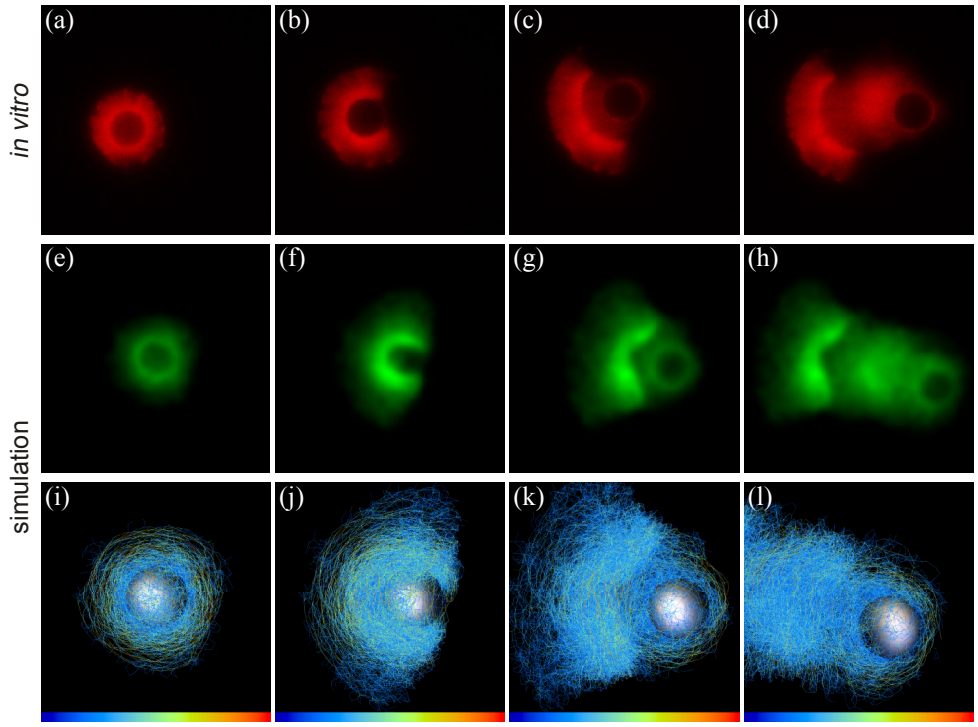

Figure 2

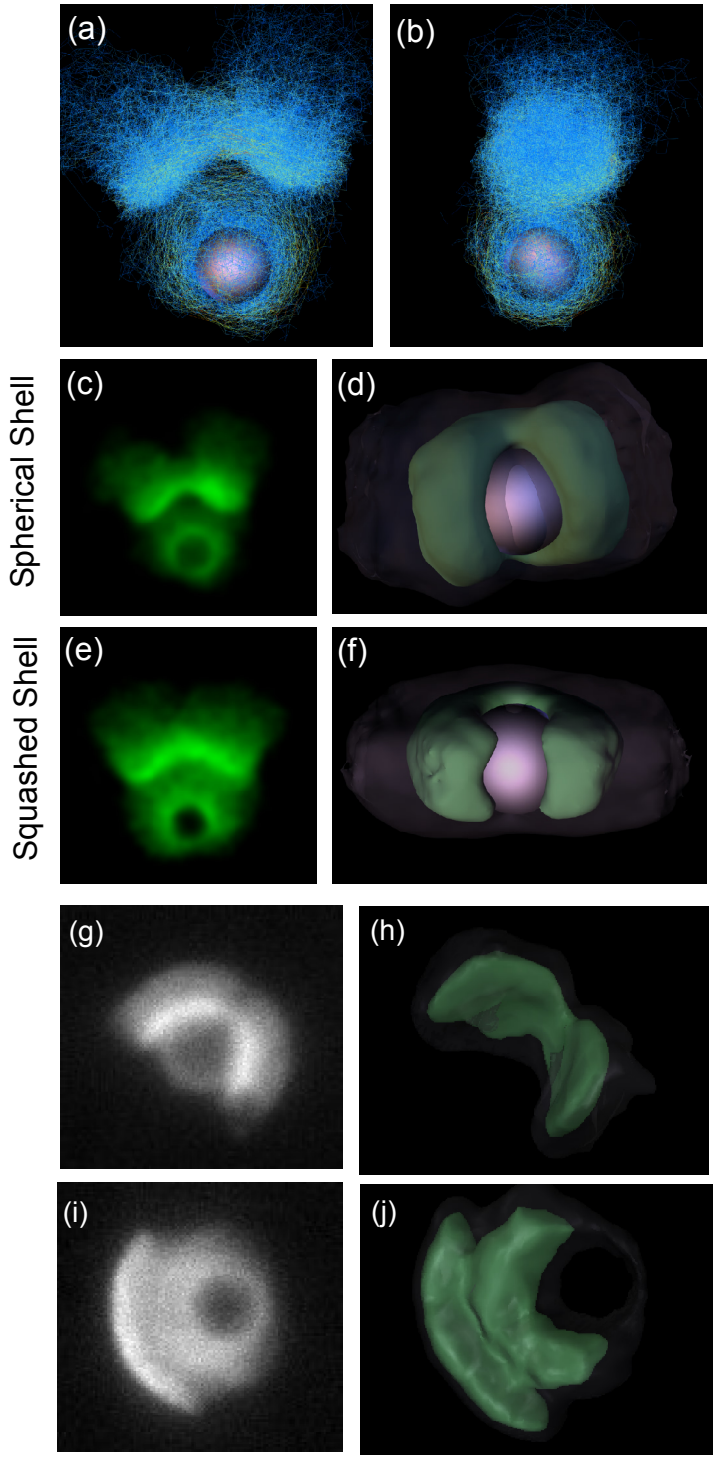

Figure 3

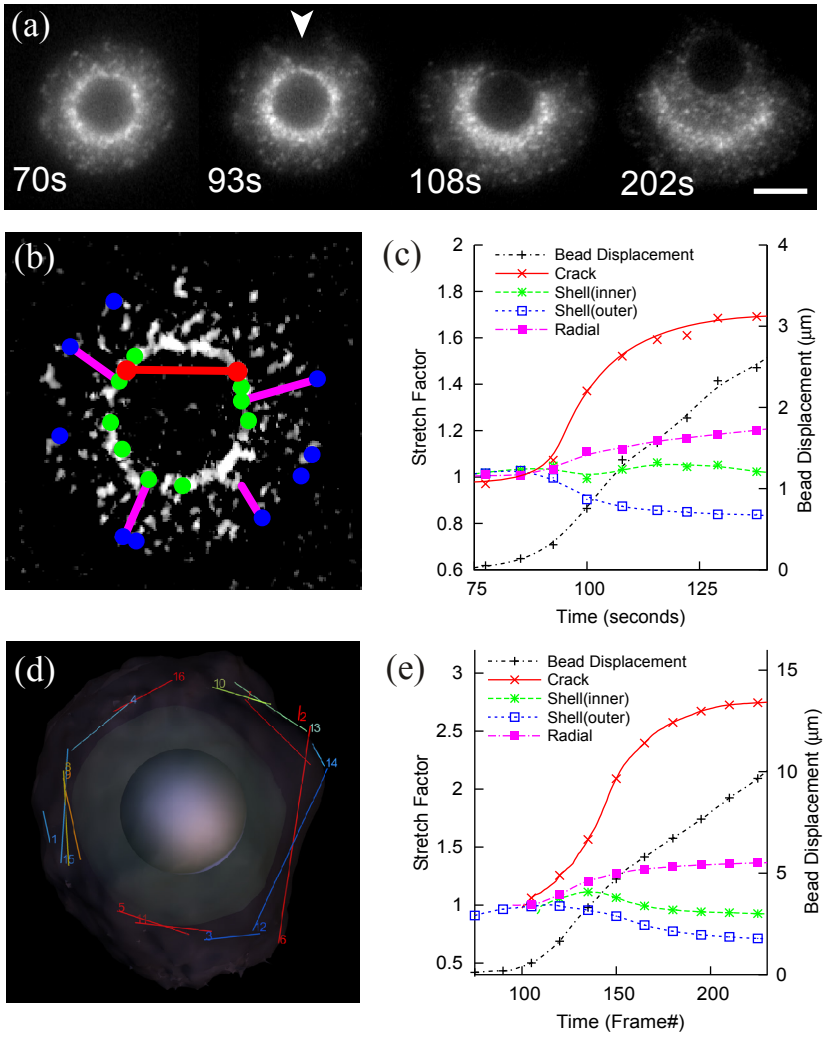
(a)
70s
93s
108s
202s
(b)
(c)
Bead Displacement
Crack
Shell(inner)
Shell(outer)
Radial
Stretch Factor
Bead Displacement (μm)
Time (seconds)
(d)
(e)
Bead Displacement
Crack
Shell(inner)
Shell(outer)
Radial
Stretch Factor
Bead Displacement (μm)
Time (Frame#)

Figure 4

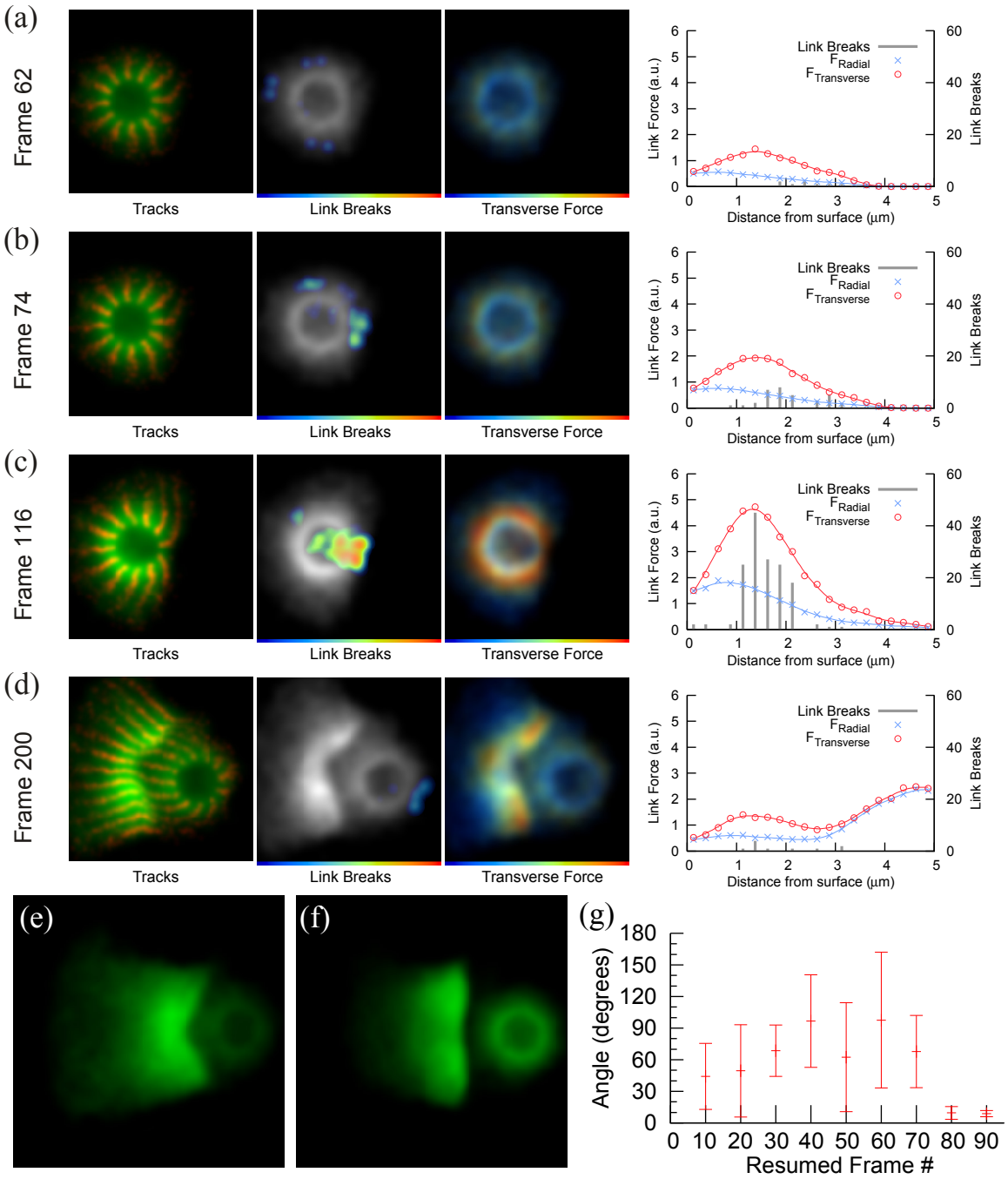
(a)
Frame 62
Tracks
Link Breaks
Transverse Force
Link Breaks
F Radial
F Transverse
Link Force (a.u.)
Link Breaks
Distance from surface (μm)
(b)
Frame 74
Tracks
Link Breaks
Transverse Force
Link Breaks
F Radial
F Transverse
Link Force (a.u.)
Link Breaks
Distance from surface (μm)
(c)
Frame 116
Tracks
Link Breaks
Transverse Force
Link Breaks
F Radial
F Transverse
Link Force (a.u.)
Link Breaks
Distance from surface (μm)
(d)
Frame 200
Tracks
Link Breaks
Transverse Force
Link Breaks
F Radial
F Transverse
Link Force (a.u.)
Link Breaks
Distance from surface (μm)
(e)
(f)
(g)
Angle (degrees)
Resumed Frame #

Figure 5

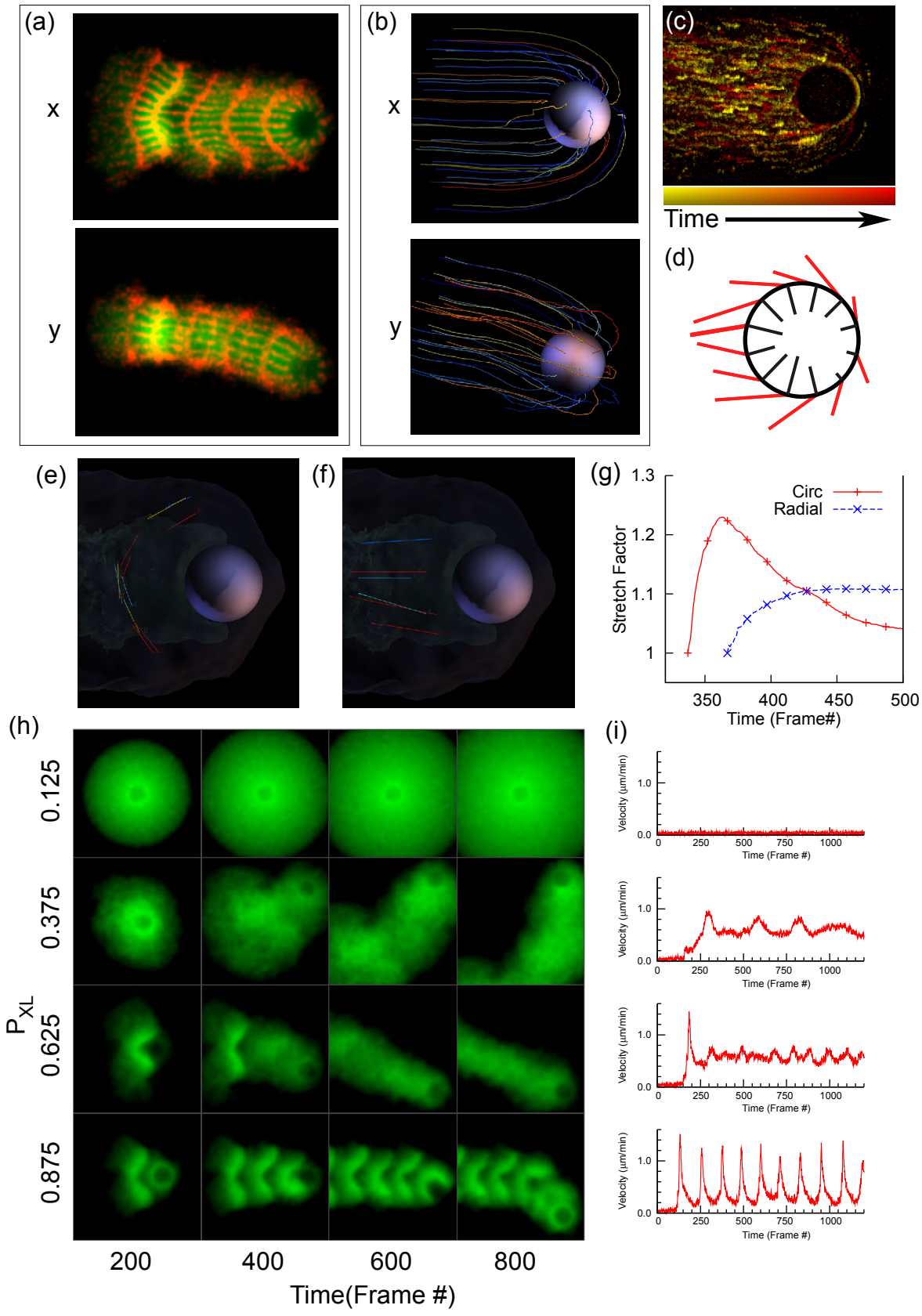
(a)
x
y
(b)
x
y
(c)
Time
(d)
(e)
(f)
(g)
Circ
Radial
Stretch Factor
1.3
1.2
1.1
1
350
400
450
500
Time (Frame#)
(h)
0.125
0.375
0.625
0.875
P_{XL}
200
400
600
800
Time(Frame #)
(i)
Velocity (μm/min)
1.0
0.0
0
250
500
750
1000
Time (Frame #)

Figure 6

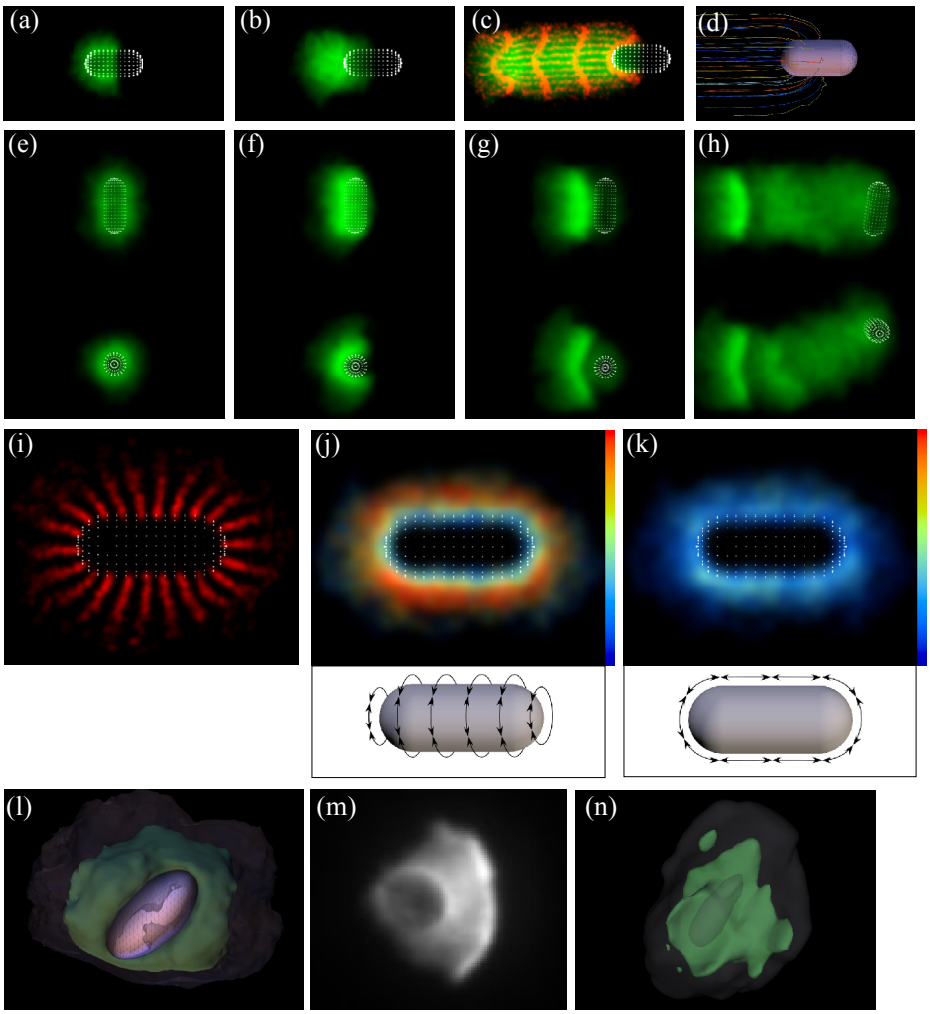

Figure 7